Nonlinear Filtering for Autonomous Navigation of Spacecraft in Highly Elliptical Orbit

Adam C. Vigneron[a,*], Anton H.J. de Ruiter[b,*], Bruce V. Burlton[a], Warren K.H. Soh[c]

[a] *Mechanical and Aerospace Engineering, Carleton University, Ottawa, Canada*
[b] *Aerospace Engineering, Ryerson University, Toronto, Canada*
[c] *Magellan Aerospace, Ottawa, Canada*

Abstract

In support of Canada's proposed Polar Communication and Weather mission, this study examined the accuracy to which GPS-based autonomous navigation might be realized for spacecraft in a Molniya orbit. A navigation algorithm based on the Extended Kalman Filter was demonstrated to achieve a three-dimensional root-mean-square accuracy of 58.9 m over a Molniya orbit with 500 km and 40 000 km perigee and apogee altitudes, respectively. Despite the inclusion of biased and non-white error models in the generated GPS pseudorange measurements – a first for navigation studies in this orbital regime – algorithms based on the Unscented Kalman Filter and the Cubature Kalman Filter were not found to improve this result; their benefits were eclipsed due to the accurate pseudorange measurements which were available during periods of highly nonlinear dynamics.

This study revealed receiver clock bias error to be a significant source of navigation solution error. For reasons of geometry, the navigation algorithm is not able to differentiate between this error and a radial position error. A novel dual-mode dynamic clock model was proposed and implemented as a means to minimize receiver clock bias error over the entire orbital regime.

Keywords: nonlinear filtering, satellite navigation, GPS modelling

1. Introduction

In response to past and current policy decisions [1], the Canadian Space Agency proposed the *Polar Communication and Weather (PCW)* mission in 2007. Two satellites will be placed in a twelve-hour Molniya orbit at the critical inclination of $i = 63.4°$. This inclination will freeze the orbit perigee in the Southern Hemisphere (cf. de Ruiter et al. [2], pp. 168–169) by cancelling the J2-driven secular perigee precession. A general expression for the secular perigee precession due to J2 may be found in Iorio [3] and a further discussion of frozen perigee orbits may be found in Kozai [4] and Lara [5]. The frozen orbit perigee will maximize the constellation's ability to provide communication and weather services to Canada's North. The operational constellation will provide continuous communication coverage north of 70°N [6] and meteorological data on a 15 minute refresh rate north of 50°N [7].

In recent years, spacecraft engineers have endeavoured to design spacecraft capable of operation at increasing levels of autonomy. Autonomous navigation solutions offer immediate availability of position and velocity estimates based on present measurements, rather than estimates based on previous ground passes. This simplifies spacecraft uplink, increases operational flexibility, and reduces ground station costs and overhead.

Autonomous navigation has been attempted and achieved by a number of spacecraft on low Earth orbit (LEO), beginning with PoSAT-1 in 1993 [8]. Though navigation for satellites in highly elliptical orbit (HEO) has not yet been achieved autonomously, past missions have demonstrated key capabilities. A classified American satellite launched in the 1990s used GPS signals to obtain a navigation solution in geostationary orbit (GEO) [9]; the solution was achieved using ground-based processing in near-real time.

* Corresponding author.
Email addresses: adam_vigneron@carleton.ca (Adam C. Vigneron), aderuiter@ryerson.ca (Anton H.J. de Ruiter)

The AMSAT-OSCAR 40 spacecraft (launched in 2000) autonomously acquired GPS signals throughout its 19-hour HEO [10]; point solutions accurate to 3 km were achieved using ground-based processing. In early 2013, the GIOVE-A navigation mission became the first civilian satellite to achieve GPS navigation (position, velocity, and time) in an orbit above the GPS constellation [11].

Since its first publication in 1960 [12], the Kalman filter and its nonlinear extensions have emerged as the de facto standard for autonomous navigation. The most common nonlinear extension of the Kalman Filter is the Extended Kalman Filter (EKF). As noted by Montenbruck [13], EKF-based filtering of GPS position fixes is a proven technology for autonomous navigation in LEO. The BIRD microsatellite (launched 2001) demonstrated real-time autonomous navigation by using GPS signals to achieve 5 m (3D RMS) position accuracy in LEO [14]. The PROBA-2 microsatellite (launched 2009) employs a commercial-off-the-shelf single-frequency GPS receiver and achieves a real-time position accuracy of 1.1 m (3D RMS) [15].

Building on LEO flight heritage, the EKF has been examined for GPS-based navigation in HEO. A 1996 study by Potti et al. [16] for the never-flown Archimedes mission featured simple dynamic and measurement models to demonstrate the feasibility of GPS-based navigation in HEO. A 2005 hardware-in-the-loop test campaign by Moreau et al. [17] utilized an RF generator, a physical receiver, and the NASA GPS-Enhanced Onboard Navigation System (GEONS) software to achieve 7 m (3D mean) position accuracy in HEO. A 2010 simulation study by Lorga et al. [18] incorporated advanced tracking algorithms and signals from the Galileo constellation to achieve < 20 m (3D 1σ) accuracy in HEO. Finally, a 2010 mathematical study by Li et al. [19] demonstrated the observability of the problem of GPS-based navigation in HEO when only one pseudorange is available for processing.

The problem of satellite navigation in HEO includes long periods of measurement outage over the apogee arc, presenting an opportunity to examine navigation in HEO using other methods of nonlinear filtering. The Unscented Kalman Filter (UKF), proposed by Julier and Uhlmann [20], is a nonlinear extension of the Kalman filter which has been shown to outperform the EKF for highly nonlinear systems with sparse measurements. A study by Choi et al. [21] examined the UKF for autonomous navigation in LEO and demonstrated that frequent measurement updates tend to minimize the benefit of the UKF over the simpler EKF. The Cubature Kalman Filter (CKF), proposed by Arasaratnam and Haykin [22], is another nonlinear extension of the Kalman filter which seeks to address the shortcomings of the EKF and UKF for specific nonlinear problems. Both of these filters will be examined against the proven EKF to determine their suitability for GPS-based navigation in HEO, where measurements are expected to be sparse over the apogee arc of the orbit.

2. Problem Formulation

2.1. Orbit dynamical model

In this study, the satellite was modelled as point mass with a state vector composed of the satellite's position, velocity, GPS receiver clock bias, and GPS receiver clock drift:

$$\mathbf{x}(t) = \left[\mathbf{r}(t)^T \ \mathbf{v}(t)^T \ b(t) \ d(t)\right]^T \tag{1}$$

The dynamical model then takes the form of a differential equation:

$$\dot{\mathbf{x}} = \mathbf{f}(\mathbf{x}, t) \tag{2}$$

with initial orbit condition given in Table 1. Dynamically, the function $\mathbf{f}(\mathbf{x}, t)$ is composed of two major accelerations: Earth gravity and third-body gravity. Atmospheric drag, solar radiation pressure, and other accelerations were examined but were not found to be significant (Vigneron [23], Sec. 2.2.5 and 5.2.4), agreeing with the findings of Montenbruck et al. [13].

The dynamical models used in this study are summarized below. All necessary ephemerides and frame rotations were obtained from the JPL Developmental Ephemeris (DE 421) [24]. Dynamical constants are summarized in Table 2. Both models were verified using truth orbits generated by AGI STK 9.2.0; truth orbit configuration details are listed in Table 3. The verification campaign revealed that the combined dynamical model matched the truth orbit to within three metres after two orbits (twenty-four hours) of propagation; further details are available in Vigneron [23] (Sec. 2.3).

Table 1: Initial Conditions for Molniya Orbit.

semi-major axis	a	26 553.4 km
eccentricity	e	0.740969
inclination	i	63.400°
right ascension of ascending node	Ω	108.208°
argument of perigee	ω	270.000°
true anomaly	ν	0.000°
epoch	t_0	00:00:00 UTC, 04 Apr 2012

Earth gravity. The high-fidelity gravitational acceleration of the Earth is compactly represented as a spherical harmonic expansion – see, e.g., Vallado [25] (p. 543). This study employed a 10×10 EGM-96 geoid on the WGS-84 ellipsoid; the older ellipsoid was retained as it is the datum used by the GPS constellation.

Third-body gravity. Earth-orbiting satellites are influenced by the gravitational pull of other bodies in the Solar System. This study used the the standard point mass approach (cf. Berry and Coppola [26]) to include the gravitational effects of the Sun and the Moon. Other bodies in the Solar System were not found to produce a significant gravitational force; see Vigneron [23] (Sec. 2.2.2) for further details.

Table 2: Propagator Constants and Parameters

Ellipsoidal Constants (WGS-84)			
Earth gravitational parameter	$\mu_\oplus$	398600.4418	$\mathrm{km^3 s^{-2}}$
radius of Earth	$R_\oplus$	6378.1370	km
Luni-Solar Constants (JPL DE-421)			
Sun gravitational parameter	$\mu_\odot$	$132.712\,440\,040\,9 \times 10^9$	$\mathrm{km^3 s^{-2}}$
Moon gravitational parameter	$\mu_\leftmoon$	$4.902\,800\,076\,228 \times 10^3$	$\mathrm{km^3 s^{-2}}$

Table 3: STK 9.2.0 HPOP Force Models (used for the truth orbit)

Earth Gravity	▸ model: EGM-96 ▸ 70 × 70
Third-Body Gravity	▸ model: point-mass ▸ Sun & Moon included

2.2. Clock dynamical model

The function $\mathbf{f}(\mathbf{x}, t)$ in (2) also contains the dynamics of the GPS receiver clock bias, b, and drift, d. This study adopted a hybrid model for receiver clock propagation representing two distinct modes of clock operation: a *steered* clock is constantly being adjusted to track GPS time within measurement error, while a *drifting* clock evolves according to stochastic processes without any adjustment by the receiver[1].

Clock-steering occurs when the receiver has lock on at least four GPS Space Vehicles (SVs) and the SVs have a favourable geometry relative to the receiver[2]. Based on results from a study by Montenbruck [28] (Fig. 3.2) this study adopted a coloured noise model for the steered receiver clock:

$$\dot{b} = -\frac{1}{\tau_s}\, b + w_s \tag{3}$$

[1] As dicussed by Mikhailov and Vasil'ev [27], the deterministic clock models suited to the highly stable clocks onboard the GPS SVs are not suitable for less accurate receiver clocks. A stochastic model is thus the model of choice.

where $\tau_s = 200\,\mathrm{s}$ is a coloured noise decay constant and w_s is a zero-mean white noise process with standard deviation $\sigma_s = 2\,\mathrm{ns}$. In this mode of clock operation, the drift is not modelled and is dropped from the state vector.

For the drifting clock, this study employed a model presented by Dainty et al. [29] appropriate for ovenized crystal clocks typically used on spaceborne GPS receivers. It is formulated as:

$$\dot{b} = d + w_b \tag{4a}$$

$$\dot{d} = w_d \tag{4b}$$

where the zero-mean white noise processes w_b and w_d have standard deviations $\sigma_b = 1.6 \times 10^{-21}\,\mathrm{s}^2 \cdot \mathrm{s}^{-1}$ and $\sigma_d = 3.2 \times 10^{-21}\,\mathrm{s}^2 \cdot \mathrm{s}^{-3}$, respectively.

As with the orbit dynamics, there is a need to generate a clock truth from which simulated measurements are derived. The clock truth is generated using (3) and (4) with the stated parameter values (τ_s, σ_s, σ_b, σ_d). The filter uses clock dynamic equations of the same form, but each parameter is assigned a random error at runtime with a standard deviation of ten percent of the parameter value.

2.3. Measurement model

In this study, measurements are formally treated as functions of state:

$$\mathbf{y} = \mathbf{h}(\mathbf{x}, t) \tag{5}$$

where measurements $\mathbf{y}$ are obtained from state vector $\mathbf{x}$ and time t through the vector function $\mathbf{h}$. This study distinguishes between *truth* measurement models $\mathbf{y}$ and *filter* measurement models $\mathbf{h}(\hat{\mathbf{x}}, t)$; the former are used by the simulation to generate measurements while the latter are used by the filter to analyze simulated measurements and rely on the filter state estimate $\hat{\mathbf{x}}$.

Hill [30] compiled a list of potential satellite-based measurements suitable for autonomous navigation. Building from these results and the flight heritage discussed in Section 1, this study examined two measurements of interest: spaceborne GPS pseudorange measurements and passive ranging from ground-based beacons. As GPS pseudoranges are the primary measurement of interest, the latter measurement will be discussed at the end of this section.

The truth and filter measurement models are defined as:

$$\mathbf{y} = \mathbf{y}_{GPS} + \Delta\mathbf{y}_{iono} + \Delta\mathbf{y}_{SV\,clk} \tag{6}$$

$$\mathbf{h}(\hat{\mathbf{x}}, t) = \mathbf{h}^{\Delta}_{GPS}(\hat{\mathbf{x}}, t) + \mathbf{h}_{iono}(\hat{\mathbf{x}}, t) \tag{7}$$

where each component is defined in Table 4 and further discussed below.

Pseudoranges and SV ephemeris error. The pseudorange to a given GPS space vehicle (SV) is a function of the receiver position $\mathbf{r}(t)$, the receiver clock bias, and the position of the ith SV $\mathbf{r}_{SV(i)}(t_b)$ at the time of broadcast. There will be one pseudorange measurement for each SV for which the receiver has lock; thus, the truth measurement model takes the form:

$$\mathbf{y}_{GPS} = \mathrm{col}_i \left[|\mathbf{r}(t) - \mathbf{r}_{SV(i)}(t_b)| \right] + c \cdot \mathrm{col}_i [\, b \,] \tag{8}$$

where c is the speed of light and col_i denotes a column vector where the ith row is given inside the brackets. The position of each SV as a function of time, $\mathbf{r}_{SV(i)}(t)$, is determined using a GPS simulator, the Navigation Laboratories LabPro-4000. Further details on the operation of the GPS simulator can be found in Appendix C of Vigneron [23].

[2]Specifically, the Time Dilution of Precision (TDOP) must be below a threshold of 10. The geometry of the HEO orbit causes the TDOP to sharply increase as the spacecraft approaches apogee. For pseudoranges accurate to within 10 m, a TDOP threshold of 10 corresponds to clock accuracies in the hundreds of nanoseconds. This is the demonstrated accuracy of the drifting clock estimation algorithm in this study; thus, anytime the TDOP threshold is exceeded it is better to estimate the receiver clock than to steer it. For further details, please see Appendix A.3 of Vigneron [23].

Table 4: Summary of measurement errors and models for GPS pseudorange

SV ephemeris error	**truth**	$\mathbf{y}_{GPS}$ (8)	uses exact GPS SV ephemerides
	filter	$\mathbf{h}^{\Delta}_{GPS}(\hat{\mathbf{x}}, t)$ (9)	uses perturbed GPS SV ephemerides
SV clock error	**truth**	$\Delta\mathbf{y}_{SVclk}$ (12)	measurements perturbed by time-varying clock error
	filter		not modelled
tropospheric delay	**truth**		signals passing within 100 km are blocked
	filter		not modelled
ionospheric delay	**truth**	$\Delta\mathbf{y}_{iono}$ (10)	measurements perturbed by Klobuchar model
	filter	$\mathbf{h}_{iono}(\hat{\mathbf{x}}, t)$ (11)	measurements partially corrected

The filter must construct its own $\mathbf{r}_{SV(i)}(t)$ using parameters broadcast by the GPS constellation. However, broadcast GPS orbits are subject to inaccuracies of a few metres. This study simulates these errors by purposefully using incorrect SV locations for the filter calculation of geometric range. The filter measurement model takes the form:

$$\mathbf{h}^{\Delta}_{GPS}(\hat{\mathbf{x}}, t) = \mathrm{col}_i \left[\left| \left(\hat{\mathbf{r}}(t) - \left(\mathbf{r}_{SV(i)}(t_b) + \Delta\mathbf{r}_{SV(i)} \right) \right) \right| \right] + c \cdot \mathrm{col}_i \left[\hat{b} \right] \tag{9}$$

where $\hat{\mathbf{r}}(t)$ and $\hat{b}$ are filter state estimates and $\Delta\mathbf{r}_{SV(i)}$ is a metre-level perturbation for the ith SV orbit. These perturbations were defined using data made available by Dr. Richard Langley of the University of New Brunswick. This data gives the maximum error in each axis over the course of a day's measurements; its application in (9) therefore represents a more significant error than what would be seen in real operation. While this constant offset model does not precisely reflect what occurs in real GPS operations (where the inaccuracy varies over the two hour interval between broadcast orbit updates), it tests the ability of the navigation algorithm to handle inaccuracies in the GPS ephemerides.

Tropospheric delay. A visibility analysis performed for this orbit showed that less than 2% of available GPS signals pass within 100 km of the Earth's surface [23]. This study therefore ignores any signal transiting through the troposphere by inflating the radius of the Earth by 100 km for signal visibility calculations.

Ionospheric delay. This study makes the worst-case assumption of a single-frequency GPS receiver processing only pseudorange measurements. Therefore, accommodation must be made for ionospheric delay of GPS signals.

The truth measurement model is incorporated into the GPS simulator. The model uses the work of Klobuchar [31] as a basis. It first calculates the ground-based ionospheric delay T_{klob} predicted by Klobuchar's model. The simulator then calculates an obliquity factor OF based on the current geometry between the satellite, the ith transmitting SV, and the Earth. The obliquity factor reflects the fact that the GPS signal is not transiting the ionosphere in a zenith-nadir sense [23]. T_{klob} and OF are combined to produce an equivalent pseudorange delay of up to 20 m at the perigee altitude of 500 km. This takes the mathematical form:

$$\Delta\mathbf{y}_{iono} = c \cdot \mathrm{col}_i \left[T_{klob} \cdot OF \right] \tag{10}$$

The filter measurement model also relies on the work of Klobuchar, whose algorithm has a demonstrated ability to remove 40–80% of the ionospheric delay. The simulation is initialized with an *ionosphere factor* IF, a randomly selected value from the range [0.4–0.8] representing the accuracy of the ionospheric model on a given day. The filter model for ionospheric delay takes the form:

$$\mathbf{h}(\hat{\mathbf{x}}, t) = IF \cdot c \cdot \mathrm{col}_i \left[T_{klob} \cdot OF \right] \tag{11}$$

In short, the filter model removes a portion of the delay that the truth model introduces, mimicking the actual performance of the Klobuchar model for a single-frequency user.

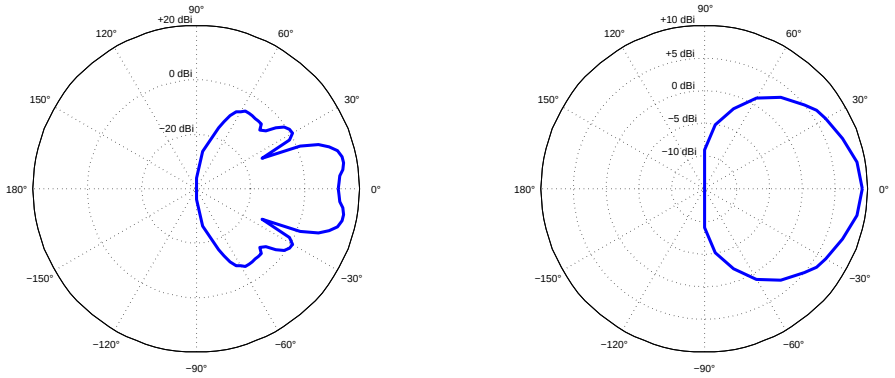

Transmitter **Receiver**

Figure 1: GPS antenna gains

SV clock errors. This study simulates errors in the SV clock-correction by perturbing the broadcast correction coefficients to produce a perturbed measurement. Based on the standard clock-correction equation (GPS Interface Specification [32], paragraph 20.3.3.3.3.1) the truth measurement model takes the form:

$$\Delta \mathbf{y}_{SV\,clk} = c \cdot \mathrm{col}_i \left[\Delta a_{f0,i} + \Delta a_{f1,i} (t_{GPS} \bmod 7200\,\mathrm{s}) + \Delta a_{f2,i} (t_{GPS} \bmod 7200\,\mathrm{s})^2 \right] \tag{12}$$

where the values $\Delta a_{fj,i}$ are the clock correction perturbations, and the 7200 s modulo operation represents the resetting of the clock-correction parameters every two hours. The clock correction perturbations were defined using data made available by Dr. Richard Langley of the University of New Brunswick; further details are available in Vigneron [23] (App. E). While this does not precisely model the true behaviour of clock-correction errors, it does test the ability of the navigation solution to handle realistic clock-correction inaccuracies.

SV visibility and link budget. In this study, an SV was considered "locked" when it passed two criteria: geometric visibility and the link budget. Geometric visibility is a straightforward calculation to ascertain whether the Earth[3] is blocking the line-of-sight vector between the receiver and the SV in question. The link budget was an adapted version of the model presented by Wertz and Larson [33] (p. 551) and used parameters and antenna gains established by a Magellan Aerospace study [34].

Transmitter power was set at 10 dB · W, noise temperature at 300 K, and receiver threshold[4] at 35 dB · Hz. The transmitter and receiver antenna gains are visualized in Figure 1. The transmitter antenna aboard each SV is nadir-pointing, while the receiver antenna aboard the spacecraft can be configured in the GPS simulator to point towards zenith, nadir, or to evolve with the spacecraft attitude.

To validate the link budget and the SV ephemerides output from the GPS simulator, two test cases were conducted. The first test case assumed a nadir-pointing receiver antenna while the second test case assumed a zenith-pointing receiver antenna. The visibility plots for these test cases (Figure 2) demonstrate that the nadir-pointing case provides better signal reception over the entire orbit. This conclusion matches that from Figures 3–3 and 3–4 of the Archimedes study by Potti et al. [16], strongly validating the link budget and SV ephemerides.

2.4. Additional measurement model: Passive Ranging

Ground-based beacons are a proven technology for autonomous satellite navigation; the CNES-led DORIS system employs a global network of transmitters to achieve onboard real-time positioning to decimetre-level accuracy [36]. However, navigation with such beacons has not yet been demonstrated beyond LEO. This study considers their inclusion as a new measurement type for HEO.

[3] and its atmosphere; see Section 2.3 for details.

[4] A more refined simulation would use separate thresholds for signal acquisition and signal tracking; see Weill [35] for further details and Potti et al. [16] for thresholds appropriate for HEO.

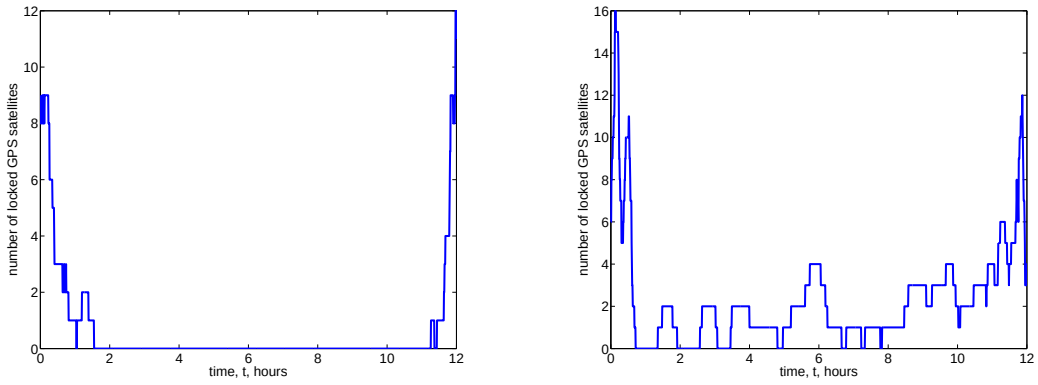

Figure 2: GPS SV visibility over a single Molniya orbit for a single GPS antenna. Perigee is located at 0 h and 12 h.

This study assumes that two beacons are in operation at existing CSA ground stations in Québec and Saskatchewan. It is also assumed that a high-quality dual-frequency GPS receiver would be co-located with the beacon; the beacons will then be able to broadcast ranging error corrections using tropospheric models [37], ionospheric models [38], and the time and position corrections available through GDGPS Bar-Sever et al. [39]. Valid signals must satisfy geometric considerations (specifically, an above-horizon constraint of 10°) and the link budget, including a transmitter profile identical to that of the GPS constellation. Simulated measurements were subject to receiver clock error derived from the same clock used in the GPS receiver.

In effect, two additional GPS satellites have been fixed to the surface of the Earth to broadcast outward. This was done in an attempt to minimize the additional hardware[5] and software required for a passive ranging implementation. The scenario outlined above preserves the autonomous nature of the navigation solution and is achievable with standard ground- and space-based components.

2.5. Other Measurement Sources

The consideration of other measurement sources appropriate for navigation was limited by the instrument suite baselined for the PCW mission. An internal study completed for PCW by Magellan Aerospace [40] demonstrated that the navigation solution was not improved by incorporating angular measurements of the Earth, Sun, and Moon obtained from the baseline attitude sensors. Other sensors (e.g. satellite laser ranging, DORIS, optical methods such as the combined Earth-/star sensor examined by Kühl [41]) were not included in the PCW baseline and were therefore not considered in this study.

For similar reasons, the reception of signals from alternative Global Navigation Satellite Systems (GNSSs) – such as GLONASS, BeiDou, and Galileo – was also not examined. A study by Qiao et al. [42] examined multi-GNSS navigation for a 10.5 h HEO orbit (perigee altitude 349 km, apogee altitude 35 800 km) similar to the Molniya orbit considered in this paper. Qiao's inclusion of four separate GNSS constellations ensured that four or more SVs were nearly always visible; brief periods with less than four SVs did occur, but never less than two and never longer than 20 min. A four-constellation solution would therefore have better SV visibility and would be less reliant on the clock modelling techniques outlined in Sections 2.2 and 2.3.

3. Kalman Filter Algorithms

This study employed three nonlinear derivatives of the Kalman Filter: the Extended Kalman Filter (EKF), the Unscented Kalman Filter (UKF), and the Cubature Kalman Filter (CKF). This section summarizes the algorithms used for each filter and extends the UKF and CKF by including their continuous-discrete (CD) implementations (CDUKF and CDCKF, respectively). For further information, please consult an appropriate textbook (e.g. Crassidis and Junkins [43], Simon [44]).

[5] Additional receiver hardware would be required as the beacons would operate on a frequency different from that of the GPS constellation.

The system is assumed to have the form[6]:

$$\dot{\mathbf{x}}(t) = \mathbf{f}\big(\mathbf{x}(t), t\big) + \mathbf{w}(t) \tag{13a}$$

$$\mathbf{y}(t_k) = \mathbf{h}\big(\mathbf{x}(t_k), t_k\big) + \mathbf{v}(t_k) \tag{13b}$$

where t_k are the sample times and the error in the dynamical and measurement equations is now formalized as $\mathbf{w}(t)$ and $\mathbf{v}(t_k)$. These error functions are zero-mean white noise signals with covariances $\mathbf{Q}(t)$ and $\mathbf{R}(t_k)$, respectively.

3.1. Extended Kalman Filter

The EKF is the *de facto* standard for nonlinear state estimation. It applies the linear Kalman filter equations through a first-order Taylor expansion of the functions $\mathbf{f}(\mathbf{x}, t)$ and $\mathbf{h}(\mathbf{x}, t)$ about a reference trajectory which follows the noise-free dynamics ($\mathbf{w} = \mathbf{0}$ or $\mathbf{v} = \mathbf{0}$, as appropriate). These first-order expansions (Jacobians) are analytical expressions which are derived from the physical model and measurement model:

$$\mathbf{F}\big(\mathbf{x}(t), t\big) = \frac{\partial}{\partial \mathbf{x}} \mathbf{f}(\mathbf{x}, t) \qquad\qquad \mathbf{H}\big(\mathbf{x}(t), t\big) = \frac{\partial}{\partial \mathbf{x}} \mathbf{h}(\mathbf{x}, t) \tag{14}$$

Using these definitions, the algorithm takes the form:

EKF Algorithm

Time update:

$$\hat{\mathbf{x}}_k^- = \hat{\mathbf{x}}_{k-1}^+ + \int_{t_{k-1}}^{t_k} \mathbf{f}\big(\hat{\mathbf{x}}(\tau), \tau\big)\, \mathrm{d}\tau \Big|_{\hat{\mathbf{x}}(t_{k-1}) = \hat{\mathbf{x}}_{k-1}^+} \tag{15a}$$

$$\boldsymbol{\Phi}(t_k, t_{k-1}) = \exp\big[\mathbf{F}(\hat{\mathbf{x}}_{k-1}^+, t_{k-1}) \cdot (t_k - t_{k-1})\big] \tag{15b}$$

$$\mathbf{P}_k^- = \boldsymbol{\Phi}(t_k, t_{k-1}) \mathbf{P}_{k-1}^+ \boldsymbol{\Phi}(t_k, t_{k-1})^T + \mathbf{Q}_{k-1} \tag{15c}$$

Measurement update:

$$\mathbf{K}_k = \mathbf{P}_k^- \mathbf{H}(\hat{\mathbf{x}}_k^-, t_k)^T \big[\mathbf{H}(\hat{\mathbf{x}}_k^-, t_k) \mathbf{P}_k^- \mathbf{H}(\hat{\mathbf{x}}_k^-, t_k)^T + \mathbf{R}_k\big]^{-1} \tag{15d}$$

$$\hat{\mathbf{x}}_k^+ = \hat{\mathbf{x}}_k^- + \mathbf{K}_k \big[\mathbf{y}_k - \mathbf{h}(\hat{\mathbf{x}}_k^-, t_k)\big] \tag{15e}$$

$$\mathbf{P}_k^+ = \big[\mathbf{I} - \mathbf{K}_k \mathbf{H}(\hat{\mathbf{x}}_k^-, t_k)\big] \mathbf{P}_k^- \big[\mathbf{I} - \mathbf{K}_k \mathbf{H}(\hat{\mathbf{x}}_k^-, t_k)\big]^T + \mathbf{K}_k \mathbf{R}_k \mathbf{K}_k^T \tag{15f}$$

where $\mathbf{K}_k$ is the Kalman gain, $\mathbf{I}$ is an appropriately sized identity matrix, $\mathbf{x}(t_k)^-$ is concisely represented by $\mathbf{x}_k^-$, and the covariances $\mathbf{Q}(t)$ and $\mathbf{R}(t_k)$ are represented by their discrete time equivalents $\mathbf{Q}_{k-1}$ and $\mathbf{R}_k$. Note that the form of (15b) assumes that $\mathbf{F}\big(\hat{\mathbf{x}}(t), t\big)$ does not significantly change over the interval $(t_k - t_{k-1})$.

The EKF is a straightforward means by which to apply the Kalman filter algorithm to a non-linear system. It has successfully been applied to many different estimation problems. However, its fundamental basis on a linearization about a reference trajectory requires that estimation errors remain small for accurate filter operation. This motivates the examination of the UKF and CKF for the current estimation problem, as both of these filters preserve nonlinearities in the dynamic and measurement models.

3.2. Unscented Kalman Filter

An alternative filter which takes greater care to preserve the non-linearities of the dynamical and measurement models is the Unscented Kalman Filter (UKF), first proposed by Julier and Uhlmann [20]. The

[6]Note that this system has no input term. This is due to two factors. First, the system considered in this study is not controlled. Second, the inclusion of a control term would not affect the performance of the filter as the control term does not appear in the estimation error dynamics.

UKF retains the EKF architecture but avoids the need for Jacobians by means of the unscented transform. This transform replaces state estimate $\hat{\mathbf{x}}$ and state covariance $\mathbf{P}$ with a set of sigma points $\mathcal{X}_i$. Each of these points is passed through the nonlinear function $\mathbf{f}(\mathbf{x}, t)$ to obtain transformed sigma points $\mathcal{F}_i$. The mean and covariance of these transformed sigma points are then calculated to obtain the transformed state and its covariance.

Using the scaled unscented transform[7], the UKF algorithm takes the form:

UKF Algorithm

1. Choose scaled unscented transform parameters α, κ, and β, and calculate:

$$\lambda = \alpha^2(n + \kappa) - n \tag{16a}$$

   where λ is a scaling parameter and n is the dimension of $\mathbf{x}$.

2. Perform the upper Cholesky decomposition (analogous to a matrix square root) of the state covariance, $\mathbf{S}^+_{k-1} = \text{chol}(\mathbf{P}^+_{k-1})$, and calculate the sigma points:

$$\begin{aligned} \mathcal{X}^+_{0,k-1} &= \hat{\mathbf{x}}^+_{k-1}, \\ \mathcal{X}^+_{i,k-1} &= \hat{\mathbf{x}}^+_{k-1} + \sqrt{n + \lambda} \cdot \mathbf{s}^+_{k-1,i}, \\ \mathcal{X}^+_{i+n,k-1} &= \hat{\mathbf{x}}^+_{k-1} - \sqrt{n + \lambda} \cdot \mathbf{s}^+_{k-1,i}, \quad i = 1, ..., n \end{aligned} \tag{16b}$$

   where $\mathbf{s}^+_{k-1,i}$ is the ith column of $\mathbf{S}^+_{k-1}$.

3. Propagate the sigma points to obtain:

$$\mathcal{F}_i = \hat{\mathbf{x}}^+_{k-1} + \int_{t_{k-1}}^{t_k} \mathbf{f}\big(\hat{\mathbf{x}}(\tau), \tau\big)\, \mathrm{d}\tau \Big|_{\hat{\mathbf{x}}(t_{k-1}) = \mathcal{X}^+_{i,k-1}}, \quad i = 0, ..., 2n \tag{16c}$$

4. Evaluate the a priori state estimate and covariance:

$$\hat{\mathbf{x}}^-_k = \sum_{i=0}^{2n} w^m_i \mathcal{F}_i \tag{16d}$$

$$\mathbf{P}^-_k = \sum_{i=0}^{2n} w^c_i (\mathcal{F}_i - \hat{\mathbf{x}}^-_k)(\mathcal{F}_i - \hat{\mathbf{x}}^-_k)^T + \mathbf{Q}_{k-1} \tag{16e}$$

   where

$$w^m_0 = \frac{\lambda}{n + \lambda}, \quad w^c_0 = w^m_0 + 1 - \alpha^2 + \beta, \quad w^m_j = w^c_j = \frac{1}{2(n + \lambda)}, \quad j = 1, ..., 2n \tag{16f}$$

5. Perform the upper Cholesky decomposition $\mathbf{S}^-_k = \text{chol}(\mathbf{P}^-_k)$, and calculate the sigma points:

$$\begin{aligned} \mathcal{X}^-_{0,k} &= \hat{\mathbf{x}}^-_k, \\ \mathcal{X}^-_{i,k} &= \hat{\mathbf{x}}^-_k + \sqrt{n + \lambda} \cdot \mathbf{s}^-_{k,i}, \\ \mathcal{X}^-_{i+n,k} &= \hat{\mathbf{x}}^-_k - \sqrt{n + \lambda} \cdot \mathbf{s}^-_{k,i}, \quad i = 1, ..., n \end{aligned} \tag{16g}$$

6. Transform the sigma points to obtain:

$$\mathcal{Y}_{i,k} = \mathbf{h}(\mathcal{X}^-_{i,k}, t_k), \quad i = 0, ..., 2n \tag{16h}$$

   and evaluate the estimated measurement, the estimated measurement covariance, and the estimated

[7] The scaled unscented transform includes additional parameters, allowing further optimization of the unscented transform for a given application [45]. These parameters will be further discussed in Section 4.6.

state-measurement variance:

$$\hat{\mathbf{y}}_k = \sum_{i=0}^{2n} w_i^m \mathcal{Y}_{i,k} \tag{16i}$$

$$\mathbf{P}_{yy,k} = \sum_{i=0}^{2n} w_i^c (\mathcal{Y}_{i,k} - \hat{\mathbf{y}}_k)(\mathcal{Y}_{i,k} - \hat{\mathbf{y}}_k)^T + \mathbf{R}_k \tag{16j}$$

$$\mathbf{P}_{xy,k} = \sum_{i=0}^{2n} w_i^c (\mathcal{X}_{i,k}^- - \hat{\mathbf{x}}_k^-)(\mathcal{Y}_{i,k} - \hat{\mathbf{y}}_k)^T \tag{16k}$$

7. Evaluate the a posteriori state estimate and covariance:

$$\hat{\mathbf{x}}_k^+ = \hat{\mathbf{x}}_k^- + \mathbf{K}_k(\mathbf{y}_k - \hat{\mathbf{y}}_k) \tag{16l}$$

$$\mathbf{P}_k^+ = \mathbf{P}_k^- - \mathbf{K}_k \mathbf{P}_{yy,k} \mathbf{K}_k^T \tag{16m}$$

where

$$\mathbf{K}_k = \mathbf{P}_{xy,k} \mathbf{P}_{yy,k}^{-1} \tag{16n}$$

Cubature Kalman Filter. A more recent reformulation of the Kalman Filter for nonlinear systems is the Cubature Kalman Filter (CKF) proposed by Arasaratnam and Haykin [22]. The CKF uses a spherical-radial cubature rule to approximate the integrals necessary to pass a Gaussian probability distribution through a nonlinear transformation. In the CKF, the chosen cubature rule results in $2n$ cubature points defined in the same fashion as the sigma points in the UKF.

CKF Algorithm

For brevity, the CKF algorithm is omitted from this paper as it is nearly identical to the UKF algorithm. The CKF algorithm can be obtained from the UKF algorithm above by setting $\alpha = 1$, $\kappa = 0$, and $\beta = 0$. These parameters result in uniform sigma point weights $w_j^m = w_j^c = (2n)^{-1}$ for $j = 1, ..., 2n$ and a suppressed central sigma point ($w_0^m = w_0^c = 0$).

3.3. Continuous-Discrete Kalman Filtering

Following the example of Särkkä [46], this paper will also examine the use of continuous dynamics for the physical model in a UKF and CKF. Since the actual process dynamics are continuous, this continuous model will provide a more accurate propagation of the mean and covariance than the discrete propagation in (16d) and (16e) at an increased computational cost.

The algorithm for continuous time propagation is outlined below. When this algorithm takes the place of (16b) through (16f), a new method of filtering is achieved where the time update is performed in continuous time and the measurement update is performed in discrete time. This filter is known as the Continuous-Discrete Unscented Kalman Filter (CDUKF). By replacing the sigma points and weights with cubature points and weights a Continuous-Discrete Cubature Kalman Filter (CDCKF) is realized.

Continuous Time Propagation for the CDUKF and CDCKF

1. Define the sigma points in continuous time:

$$\begin{aligned} \mathcal{X}_0 &= \hat{\mathbf{x}}, \\ \mathcal{X}_i &= \hat{\mathbf{x}} + \sqrt{n+\lambda} \cdot \mathbf{s}_i, \\ \mathcal{X}_{i+n} &= \hat{\mathbf{x}} - \sqrt{n+\lambda} \cdot \mathbf{s}_i, \quad i = 1, ..., n \end{aligned} \tag{17a}$$

2. Define a continuous function $\hat{\mathbf{f}}$ which is a weighted summation of the physical model $\mathbf{f}(\mathbf{x}, t)$ applied to each sigma point:

$$\hat{\mathbf{f}} = \sum_{i=0}^{2n} w_i^m \, \mathbf{f}(\mathcal{X}_i, t) \tag{17b}$$

3. Define an intermediate matrix $\mathbf{\Gamma}$ which will be used in the time derivative of the state covariance:

$$\begin{aligned}\mathbf{\Gamma} &= \sum_{i=1}^{2n} w_i^c \left(\mathcal{X}_i - \hat{\mathbf{x}}\right)\left(\mathbf{f}(\mathcal{X}_i, t) - \hat{\mathbf{f}}\right)^T \\ &+ \sum_{i=1}^{2n} w_i^c \left(\mathbf{f}(\mathcal{X}_i, t) - \hat{\mathbf{f}}\right)\left(\mathcal{X}_i - \hat{\mathbf{x}}\right)^T \\ &+ \mathbf{Q}(t) \end{aligned} \tag{17c}$$

where $\mathbf{Q}(t)$ is the continuous process noise covariance.

4. Define a matrix function $\mathbf{\Phi}(\mathbf{A})$ which will be used in the time derivative of the state covariance:

$$\mathbf{\Phi}(\mathbf{A}) = \text{s\_triu}(\mathbf{A}) + \tfrac{1}{2}\text{diag}(\mathbf{A}) \tag{17d}$$

where $\text{s\_triu}(\mathbf{A})$ is the strictly upper triangular part of matrix $\mathbf{A}$ (i.e., the components above the main diagonal) and $\text{diag}(\mathbf{A})$ is the diagonal part of $\mathbf{A}$.

5. With the definitions above, the time derivative of state estimate $\hat{\mathbf{x}}$ and Cholesky-decomposed state covariance $\mathbf{S} = \text{chol}(\mathbf{P})$ can be related as:

$$\frac{\mathrm{d}\hat{\mathbf{x}}}{\mathrm{d}t} = \hat{\mathbf{f}}, \tag{17e}$$

$$\frac{\mathrm{d}\mathbf{S}}{\mathrm{d}t} = \mathbf{S}\mathbf{\Phi}\left(\mathbf{S}^{-1}\mathbf{\Gamma}\mathbf{S}^{-T}\right). \tag{17f}$$

6. Finally, taking all of the previous equations into account realizes the time update in continuous time:

$$\hat{\mathbf{x}}_k^- = \int_{t_{k-1}}^{t_k} \frac{\mathrm{d}\hat{\mathbf{x}}}{\mathrm{d}\tau}\,\mathrm{d}\tau \Big|_{\hat{\mathbf{x}}(t_{k-1})=\hat{\mathbf{x}}_{k-1}^+} \tag{17g}$$

$$\mathbf{S}_k^- = \int_{t_{k-1}}^{t_k} \frac{\mathrm{d}\mathbf{S}}{\mathrm{d}\tau}\,\mathrm{d}\tau \Big|_{\hat{\mathbf{x}}(t_{k-1})=\hat{\mathbf{x}}_{k-1}^+, \mathbf{S}(t_{k-1})=\mathbf{S}_{k-1}^+} \tag{17h}$$

$$\mathbf{P}_k^- = \mathbf{S}_k\mathbf{S}_k^T \tag{17i}$$

4. Nonlinear Filter Performance

The navigation solution accuracy was assessed through simulation, the bulk of which was completed in a customized MATLAB environment which accepts as inputs a truth orbit and simulated GPS measurements. The truth orbit was generated using Satellite Tool Kit (STK 9.2.0) in accordance with Tables 1, 2, and 3. The simulated GPS measurements were generated using a purpose-built GPS simulator, the LabPro-4000 from Navigation Laboratories.

The realism of this simulation is enhanced by the use of separate dynamical models for the truth orbit (obtained using STK) and the navigation filter (described in Section 2.1 and Section 2.2). The propagator discrepancies are treated as process noise stemming from differences in physical model fidelity. Great care was taken to eliminate other discrepancies, including those between physical constants and reference frames[8].

4.1. Simulation Configuration

During the simulation setup, a number of design decisions were implemented. These decisions are summarized in Table 5 and discussed further in this section.

[8]The FK5 J2000 frame was used for the calculation of the equations of motions, while the ITRF93 frame was used for the calculation of the Earth geoid acceleration. For further details, please consult Appendix A.2 of Vigneron [23].

Simulation length. The simulation runs for one twelve-hour Molniya orbit. Due to excellent GPS coverage near the Earth, the navigation solution converges to metre-level accuracy at each perigee regardless of the inaccuracies accumulated over the previous apogee arc. Thus, it is only necessary to examine the solution's behaviour as it traverses the northern arc of the Molniya orbit.

Numerical propagator. Two numerical propagators were considered: an explicit fourth-order Runge-Kutta method (see, e.g., Butcher [47]) and a built-in MATLAB function (`ode45`) realizing a fourth-order Runge-Kutta style algorithm developed by Dormand and Prince [48]. In this application, `ode45` was the integrator of choice as it matched the accuracy of the explicit fourth-order method at a fraction of the computational cost.

Initial Conditions. The initial conditions for state vector $\mathbf{x}_0^+$ were randomly generated using MATLAB's `randn` function. The necessary standard deviations can be found in Table 5. The initial state covariance $\mathbf{P}_0^+$ was initialized with the corresponding variances along the main diagonal.

Fidelity of $\mathbf{F}(\mathbf{x}, t)$. The Jacobian implemented within the EKF accounts for only the two-body acceleration and the current mode of receiver clock operation. A more complex Jacobian accounting for the J_2 effect was examined through simulation but not implemented as it was found to have no measurable impact on the solution.

Process noise. An iterative method of filter tuning resulted in the following discrete-time[9] process noise covariance matrix:

$$\mathbf{Q}_k = \begin{bmatrix} Q_r \cdot \mathbf{I}_3 & 0 & 0 \\ 0 & Q_v \cdot \mathbf{I}_3 & 0 \\ 0 & 0 & \mathbf{Q}_{clock} \end{bmatrix} \tag{18}$$

where Q_r is the position process noise, Q_v is the velocity process noise, $\mathbf{Q}_{clock}$ is the receiver clock process noise, and $\mathbf{I}_3$ is a 3×3 identity matrix. The values for Q_r and Q_v are constant[10] and can be found in Table 5. The definition of $\mathbf{Q}_{clock}$ will depend on the current mode of receiver clock operation:

- If the clock is being steered, $\mathbf{Q}_{clock} = [\sigma_{s,f}^2]$;
- If the clock is drifting, $\mathbf{Q}_{clock} = \text{diag}(\sigma_{b,f}^2, \sigma_{d,f}^2)$;

where each parameter of the filter clock model $\sigma_{i,f}$ is derived from the corresponding parameter of the truth clock model σ_i corrupted by random noise with a standard deviation of 10%: $\sigma_{i,f} = (1 + 0.1 \cdot \texttt{randn}) \cdot \sigma_i$. The values of the parameters for the truth clock model are found in Section 2.2.

Measurement frequency. Current spaceborne GPS receivers can provide raw pseudoranges at a freqency of 1 Hz – see, for example, the documented on-orbit performance of the Astrium MosaicGNSS receiver [49]. For this study, a conservative update interval of 30 s was selected to ensure the robustness of the navigation solution. This interval was found to be sufficient for LEO by Montenbruck et al. [13] in their analysis for filter-based navigation of PROBA-2.

GPS receiver channels. Following the example of the Astrium MoisaicGNSS receiver [49] this study included a maximum of eight pseudoranges in the navigation solution.

Attitude profile and antenna field-of-view. In this study, a nadir-pointing attitude was assumed over the entire HEO orbit, permitting the simulation of a single GPS receiver with a nadir antenna and a zenith antenna.

[9] The continuous-time filters will use the continuous equivalent of (18).
[10] Note that these values are specific to the 30 s measurement interval.

Measurement noise. An iterative method of filter tuning resulted in a measurement noise covariance matrix of $\mathbf{R}_k = \left[R_{GPS} \cdot \mathbf{I}_k\right]$, where $R_{GPS} = (10\,\mathrm{m})^2 + R_{iono}$ contains the tuned parameter plus an an additional positive term to improve filter performance in the presence of ionospheric error and $\mathbf{I}_k$ is an identity matrix with dimensions matching the number of currently locked satellites. In line with the discussion in Section 2.3, R_{iono} is the square of the ith component of $(1 - \overline{IF}) \cdot \mathbf{h}^t_{iono}(\mathbf{x}, t)$ where $\overline{IF}$ is the average ionosphere factor of 0.6. In effect, the filter assumes that the ionospheric model removes 60% of the ionospheric effect, when in reality it removes between 40–80%.

Table 5: Baseline Simulation Configuration

Propagator Settings	
simulation length	12 h
numerical propagator	`ode45`
initial conditions $\mathbf{x}_0^+$, $\mathbf{P}_0^+$	$r_0 = N(0, 100\,\mathrm{m})$ $v_0 = N(0, 1\,\mathrm{m \cdot s^{-1}})$ $b_0 = N(0, 1\,\mu\mathrm{s})$ $d_0 = N(0, 1\,\mu\mathrm{s \cdot s^{-1}})$
EKF Jacobian matrix $\mathbf{F}(\mathbf{x}, t)$	two-body
process noise covariance $\mathbf{Q}_k$	$Q_r = 1 \times 10^{-7}\,\mathrm{km^2}$ $Q_v = 1 \times 10^{-13}\,\mathrm{km^2 \cdot s^{-2}}$ $\mathbf{Q}_{clock}$ per (18)
Measurement Settings	
sample period	30 s
number of GPS channels	8
number of GPS antennae	2 (nadir & zenith)
measurement noise covariance $\mathbf{R}_k$	$R_{GPS} = (10\,\mathrm{m})^2$

4.2. Baseline EKF Analysis

The results of a sample simulation configured per Table 5 can be seen in Figure 3a to Figure 3f inclusive. Figure 3a to Figure 3d contain the time histories of the state errors (solid lines) and the 3σ uncertainty bounds (dashed lines) within which the errors should remain the majority of the time. Figure 3e is a layered figure that combines position error data from Figure 3a with satellite visibility data. The vertical bars indicate the number of GPS SVs being processed by the navigation solution. A white bar corresponds to zero SVs, a black bar indicates four or more, and the varying shades of grey cover the intermediate values. Figure 3f contains the 2-norm of the residuals, providing insight to the degree of accuracy with which the filter is estimating the measurements it is receiving.

Figures 3a and 3c demonstrate that the navigation solution is accurate to tens of metres in position and millimetres per second in velocity. Comparing these figures with Figure 3e provides insight into the solution: solution accuracy and uncertainty both increase over the apogee arc as GPS coverage becomes sparse, and the gradual return of coverage from the eighth hour onward is reflected by a corresponding reduction in error and uncertainty until perigee is reached

Figures 3b and 3d demonstrate that the clock dynamics also remain converged throughout the simulation. Comparing these figures with Figure 3e, it is evident that clock bias and drift only experience significant error during total GPS signal outage.

Figure 3e demonstrates that sharp changes in the navigation solution correspond directly to the acquisition of an additional GPS signal. As each GPS signal has a unique set of ephemeris and clock errors, the minimum variance state estimate will change significantly with the acquisition or loss of a GPS satellite.

All figures demonstrate that the EKF is working as expected; the solution error is constrained by the 3σ bounds and remains converged throughout the period of simulation. The final baseline plot, Figure 3f, demonstrates that upon signal acquisition, the EKF quickly forces the residual down to the magnitude of the measurement error itself. This confirms the EKF as well-suited for this application.

4.3. Effect of Receiver Clock Error

To further explore the behaviour of this navigation algorithm, simulations were performed where the receiver clock was assumed error-free. The results of a sample simulation can be seen in Figure 4a and

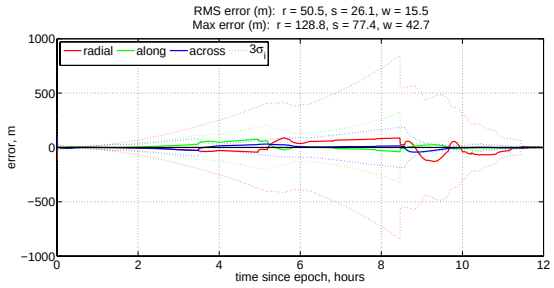

(a) Position error, along/ across/ radial frame

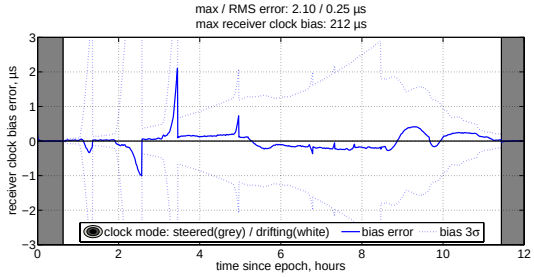

(b) Receiver clock bias error and receiver clock mode

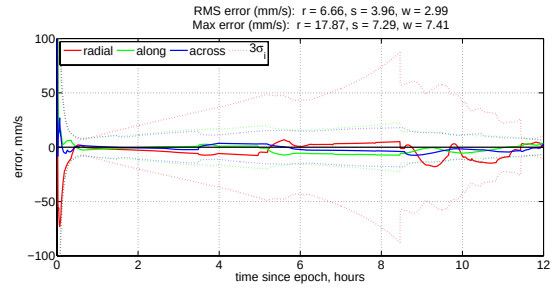

(c) Velocity error, along/across/radial frame.

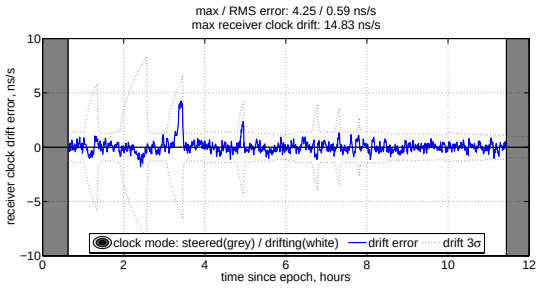

(d) Receiver clock drift error and receiver clock mode.

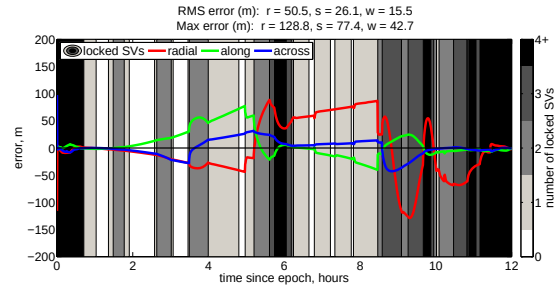

(e) Position error and locked GPS satellites.

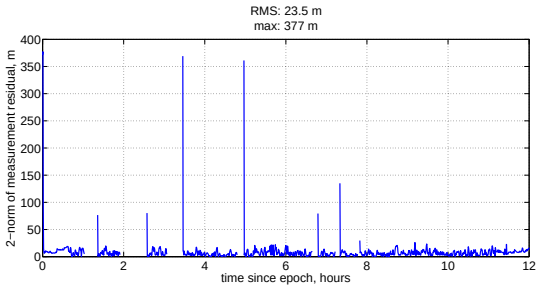

(f) Measurement residuals.

Figure 3: Baseline simulation

Figure 4b.

There is a remarkable improvement in this solution. RMS position errors drop to less than twenty metres, while no coordinate reaches an error exceeding sixty metres. Further, the solution is well-behaved; error grows during periods of propagation and shrinks (sometimes with great speed) as new measurements are processed. The solution exhibits transient divergence when new SVs are acquired (e.g., just before the 8 h mark) – as before, this results from the incorporation of uniquely biased measurements into the navigation solution.

Most interesting is the behaviour of the radial coordinate. Previously the most error-prone, it has an RMS error of a mere 4.4 m – a full order of magnitude improvement. This behaviour sheds light on the behaviour exhibited by radial position error during the baseline simulation. When the satellite is high on the apogee arc, it is only receiving signals from GPS SVs on the far side of the Earth. This line-of-sight is very nearly aligned with the Earth-centred radial direction from the along-across-radial reference frame. Thus, pseudoranges on the apogee arc are primarily functions of two factors: the radial distance plus the (scaled) receiver clock bias.

If the filter is underestimating one of these parameters, it will respond by overestimating the other one. A close examination of Figure 3a and Figure 3b between the eighth and tenth hour reveals that receiver clock bias and radial position error are indeed negatively correlated with a similar order of magnitude (recall

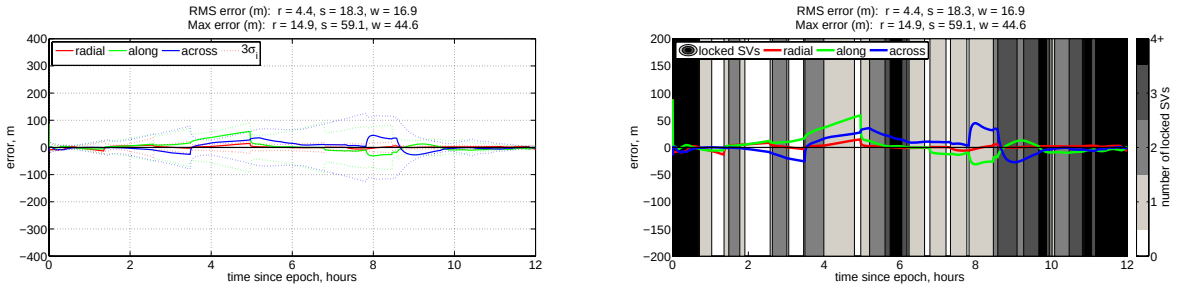

(a) Position error, along/ across/ radial frame

(b) Position error and locked GPS satellites

Figure 4: Receiver clock perfect

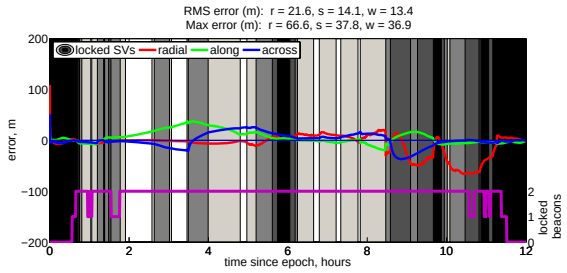

Figure 5: Navigation using passive ranging and GPS, receiver clock error included, $R_{rge} = (50\,\mathrm{m})^2$. The purple line indicates the number of beacons being processed by the navigation solution over the course of the orbit.

that 300 ns approximately corresponds to 100 m).

Thus, the residuals in Figure 3f (where residuals were seen to be well below the twenty metre threshold) are reconciled with the hundred-plus metre error in radial position between the eighth and tenth hour.

4.4. Inclusion of Passive Ranging

In an effort to improve the estimation of the radial coordinate, passive ranging measurements were fused with the GPS pseudorange measurements by the method outlined in Section 2.3. These ranging measurements were corrupted with a zero-mean white noise signal ($\sigma_{rge} = 5\,\mathrm{m}$) corresponding to the approximate error that remains after the errors listed in Section 2.3 have been accounted for (cf. United States Coast Guard [50], Table 3-1). For consistent fusion with the existing GPS measurements, these measurements will be reported on the same measurement interval of 30 s.

The inclusion of this additional measurement required an augmentation of the measurement noise covariance matrix:

$$\mathbf{R}_{GPS+rge} = \begin{bmatrix} \mathbf{R}_{GPS} & 0 \\ 0 & R_{rge} \cdot \mathbf{I}_j \end{bmatrix} \tag{19}$$

where R_{rge} is a tuning parameter and $\mathbf{I}_j$ is an identity matrix with dimensions equal to the number of currently locked beacon signals. Through a tuning process, a value of $R_{rge} = (50\,\mathrm{m})^2$ was found to be satisfactory.

The performance of the filter with beacons included can be seen in Figure 5. The continuous measurement coverage softens the transients that occur when a new GPS signal is acquired. Comparing its 3D RMS error of 29.1 m with previous simulations, a significant improvement is seen over the baseline simulation (58.9 m). Thus, the inclusion of passive ranging has been verified as a means to improve the navigation solution.

4.5. Antenna Failures

A final EKF simulation campaign examined the impact of GPS receiver antenna failures on the solution accuracy. In the event that the zenith antenna fails, GPS coverage over the apogee arc is sufficient for

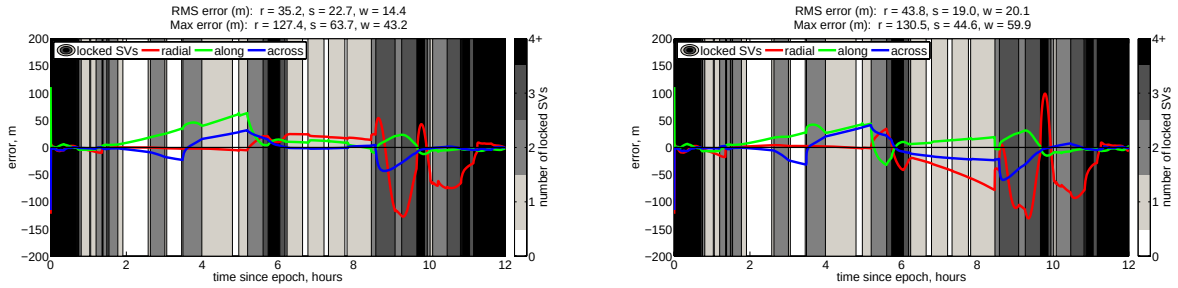

(a) Discrete UKF

(b) Continuous-Discrete UKF

Figure 6: Other nonlinear filters, position error and locked GPS satellites

Table 6: Summary of Results for Nonlinear Filters

Filter algorithm	**Radial error**	**Along error**	**Across error**	**3D RMS error**	**Computational runtime, relative**
POSITION (m)					
EKF	34.9	22.4	14.3	43.9	1
UKF	35.2	22.7	14.4	44.3	10
CKF	35.2	22.7	14.4	44.3	10
CDUKF	43.8	19.0	20.1	51.8	15
CDCKF	34.6	22.4	14.2	43.6	15
VELOCITY ($\mathrm{mm \cdot s^{-1}}$)					
EKF	6.12	3.69	3.07	7.78	1
UKF	6.08	3.70	3.08	7.76	10
CKF	6.08	3.70	3.08	7.76	10
CDUKF	7.51	3.95	3.82	9.31	15
CDCKF	6.15	3.68	3.05	7.79	15

a navigation solution accurate to 160 m (3D RMS). In the complementary case, GPS outage lasts over the entire 10 h apogee arc. The propagator is forced to act without measurement updates and maintains an accuracy of 1.42 km (3D RMS) but reconverges without difficulty once signals are re-acquired. This validates the propagator and and highlights the filter's ability to reconverge even after multiple hours without a measurement update.

4.6. Other Nonlinear Filters

Section 3 introduced a quartet of alternatives to the EKF: the Unscented Kalman Filter, the Cubature Kalman Filter, the Continuous-Discrete Unscented Kalman Filter, and the Continuous-Discrete Cubature Kalman Filter. The final set of simulations for this study will evaluate the performance of these filters against the EKF when processing only GPS pseudorange measurements.

A tuning process grounded in the literature (cf. Wan and van der Merwe [51]) resulted in the UKF parameters $\alpha = 1 \times 10^{-2}$, $\kappa = -5$, and $\beta = 2$. The results of a tuned UKF simulation can be seen in Figure 6a. This figure is visually indistinguishable from the EKF-based solution in Figure 3e); the covariance bounds (not shown) behave likewise.

In a similar fashion, the CKF, CDUKF, and CDCKF were applied to the same measurement dataset; their quantitative performance can be found in Table 6. These five simulations can be directly compared to each other, but they cannot be compared to the values from the baseline case in Section 4.2 as that simulation used a measurement dataset initialized with slightly different clock and ionospheric conditions (both are driven by random values).

Examining this table, it is evident that the accuracy of four of the five filters matches within a metre. The outlier, the CDUKF, is plotted in Figure 6b for comparison. Though this trajectory is slightly different

than the other four, it retains a similar level of accuracy and is well within the operational requirements of the PCW mission which motivated this study.

The rightmost column of Table 6 gives an indication of the computational time required for each filter when applied to our navigation problem. Exact computation times varied from run to run, but in general EKF analyses were executed in a tenth to fifteenth of the time of the other filters. This was due the simplified EKF Jacobian (cf. Section 4.1) and the need to propagate the nonlinear dynamics (including the computationally intensive gravity model) for each sigma point in the complex filters.

Section 1 showed that the UKF and CKF were not found to provide a significant improvement when implemented for GPS-based navigation for ground-based or LEO users due to the high availability of measurements. Based on the results in Table 6, it appears that these conclusions hold for GPS-based navigation in HEO. Combining this conclusion with the discussion in the previous paragraph, we conclude that for the problem of GPS-based position determination in HEO, the Extended Kalman Filter is the computationally efficient and accurate solution.

5. Conclusions

This study examined methods of nonlinear filtering for the autonomous navigation of spacecraft in highly elliptical orbits. Our primary filtering algorithm, the Extended Kalman Filter, achieved a positional accuracy of 58.9 m (3D RMS) over a single Molniya orbit. Over this time, no single component of error exceeded 130 m; this satisfies the 150 m (3σ) performance specification for our reference mission. These results were achieved in a simulation study which included error models not previously examined in the literature for GPS-based navigation in HEO, including non-white measurement errors specific to the physics and processing of pseudorange measurements.

Despite the inclusion of biased and non-white error models for the GPS pseudorange measurements, more sophisticated nonlinear filters (the Unscented Kalman Filter and the Cubature Kalman Filter) and their continuous-discrete counterparts were not found to improve on the performance of the EKF. This conclusion has its foundation in the nature of the problem itself. When the dynamics and measurements are at their most nonlinear (at perigee due to strong geoidal gravity and rapidly changing geometry) GPS coverage is excellent, allowing the measurement update to quickly correct any propagation errors. When the measurements are infrequent (at apogee), the dynamics and measurements have limited nonlinearities; specifically,the Earth gravity approaches a point source and the pseudorange measurement approaches a linear combination of the radial coordinate and the receiver clock bias.

Receiver clocks for spaceborne GPS satellites are prone to inaccuracy and require good GPS signal coverage to correct any biases that develop over time. Our HEO spacecraft is not able to fulfill this requirement and so must estimate the receiver clock bias using sporadic GPS signals which are themselves corrupted by this bias. In this study, a dual-mode receiver clock model was shown to constrain receiver clock bias with just a single measurement.

This study introduced the concept of passive ranging as a means of providing additional autonomous measurements to our spacecraft. Briefly, this concept would require a pair of beacons set up in the Northern Hemisphere broadcasting a signal that is operationally similar to that broadcast by the GPS constellation. An exploratory study of this concept showed a 50% reduction in the position error of our navigation solution over the entire Molniya orbit.

6. Acknowledgements

This study was completed as a partnership between Carleton University and Magellan Aerospace under a Canadian Space Agency (CSA) Space Technology Development Program (STDP). The authors would like to acknowledge the support of the CSA, the Natural Science and Engineering Research Council of Canada (NSERC), and the Ontario Graduate Scholarship (OGS) program.

References

[1] Governor General of Canada, Seizing Canada's moment: propserity and opportunity in an uncertain world, speech from the Throne, October 16, 2013. URL: http://www.speech.gc.ca.

[2] A. H. de Ruiter, C. J. Damaren, J. R. Forbes, Spacecraft Dynamics and Control, West Sussex: John Wiley & Sons, Ltd., 2013.

[3] L. Iorio, Perturbed stellar motions around the rotation black hole in Sgr A* for generic orientation of its spin axis, Physical Review D 84:124001 (2011).

[4] Y. Kozai, Motion of a particle with critical inclination in the gravitational field of a spheroid, Smithsonian Contribution to Astrophysics 5 (1961) 53–58.

[5] M. Lara, On inclination resonances in artificial satellite theory, Acta Astronautica 110 (2015) 239–246.

[6] Canadian Space Agency, Polar Communication and Weather mission (PCW), accessed 20 Oct 2013. URL: http://www.asc-csa.gc.ca/eng/satellites/pcw/.

[7] A. P. Trishchenko, L. Garand, Canadian Polar Communication and Weather (PCW) satellite system: new capabilities for mapping Arctic snow and ice dynamics from highly elliptical orbit, 6th EARSeL Workshop: Cryosphere, Hydrology & Climate Interactions, University of Bern, Switzerland, 2011.

[8] M. Unwin, M. Sweeting, A practical demonstration of low cost autonomous orbit determination using GPS, in: Proceedings of the 8th International Technical Meeting of the Satellite Division of the Institutite of Navigation, 1995, pp. 579–587.

[9] J. D. Kronman, Experience using GPS for orbit determination of a geosynchronous satellite, in: Proceedings of ION GPS 2000, Salt Lake City, UT, 2000, pp. 1622–1626.

[10] G. Davis, M. Moreau, R. Carpenter, F. Bauer, GPS-based navigation and orbit determination for the AMSAT AO-40 satellite, in: Proceedings of the AIAA Guidance, Navigation, and Control Conference, Monterey, CA, 2002.

[11] ESA Space Engineering, Far-out space navigation from sideways satnav signals, accessed 05 April 2014. URL: http://http://www.esa.int/Our_Activities/Space_Engineering/Far-out_space_navigation_from_sideways_satnav_signals.

[12] R. E. Kalman, A new approach to linear filtering and prediction problems, Transactions of the ASME, Journal of Basic Engineering 82 (1960) 35–45.

[13] O. Montenbruck, M. Markgraf, J. Naudet, S. Santandrea, K. Gantois, P. Vuilleumier, Autonomous and precise navigation of the PROBA-2 spacecraft, in: Proceedings of the AIAA/AAS Astrodynamics Specialists Conference, Honolulu, 2008.

[14] E. Gill, O. Montenbruck, S. Montenegro, Flight results from the BIRD onboard navigation system, in: Proceedings of the 5th International ESA Conference on GNC Systems, Frascati, 2002.

[15] O. Montenbruck, P. Swatschina, M. Markgraf, S. Santandrea, J. Naudet, E. Tilmans, Precision spacecraft navigation using a low-cost GPS receiver, GPS Solutions 16 (2012) 519–529.

[16] J. Potti, M. Bello, A. Pasetti, A GPS-based orbit positioning system for the European Archimedes mission, in: Proceedings of the Third International Conference on Spacecraft GNC Systems, 1996, pp. 67–75.

[17] M. Moreau, B. Naasz, J. Leitner, J. R. Carpenter, D. Gaylor, Hardware in-the-loop demonstration of real-time orbit determination in high Earth orbits, in: Proceedings of the ION National Technical Meeting, San Diego, 2005.

[18] J. Lorga, P. Silva, F. Dovis, A. Di Cintio, S. Kowaltschek, D. Jiminez, R. Jansson, Autonomous orbit determination for future GEO and HEO missions, in: 5th ESA Workshop on Satellite Navigation Technologies, 2010, pp. 1–14.

[19] T. Li, J. Liu, Z. Huang, H. Qin, Observability of HEO satellite autonomous navigation system using GPS, in: Proceedings of the 2010 International Conference on Multimedia Technology, Ningbo, 2010.

[20] S. J. Julier, J. K. Uhlmann, Unscented filtering and nonlinear estimation, Proceedings of the IEEE 92 (2004) 401–422.

[21] E.-J. Choi, J.-C. Yoon, B.-S. Lee, S.-Y. Park, K.-H. Choi, Onboard orbit determination using GPS observations based on the unscented Kalman filter, Advances in Space Research 46 (2010) 1440–1450.

[22] I. Arasaratnam, S. Haykin, Cubature Kalman filters, IEEE Transactioons on Automatic Control 54 (2009) 1254–1269.

[23] A. C. Vigneron, *Nonlinear Filtering for Autonomous Navigation of Spacecraft in Highly Elliptical Orbit*, Master's thesis, Carleton University, 2014.

[24] W. M. Folkner, J. G. Williams, D. H. Boggs, The planetary and lunar ephemeris DE 421, IPN Progress Report 42-178, Jet Propulsion Laboratory, 2009.

[25] D. A. Vallado, Fundamentals of Astrodynamics and Applications, 3rd ed., Hawthorne, CA: Microcosm Press, 2007.

[26] M. M. Berry, V. T. Coppola, Correct modeling of the indirect term for third-body perturbation, White paper, Analytical Graphics Inc., 2007.

[27] N. Mikhailov, M. Vasil'ev, Autonomous satellite orbit determination using spaceborne GNSS receivers, Gyroscopy and Navigation 2 (2011) 1–9.

[28] O. Montenbruck, Performance assessment of the NovAtel OEM4-G2 receiver for LEO satellite tracking, Technical Report TN 03-05, Space Flight Technology, DLR/GSOC, 2003.

[29] B. Dainty, J. Raquet, R. Beckman, Improving geostationary satellite GPS position error using dynamic two-way time transfer measurements, in: Proceedings of the 39th Annual Precise Time and Time Interval Meeting, 2007, pp. 511–530.

[30] K. A. Hill, Autonomous Navigation in Libration Point Orbits, Ph.D. thesis, University of Colorado, Boulder, 2007.

[31] J. A. Klobuchar, Ionospheric time-delay algorithm for single-frequency GPS users, IEEE Transactions on Aerospace and Electronic Systems 3 (1987) 325–331.

[32] Global Positioning Systems Directorate, Navstar GPS Space Segment / Navigation User Interfaces, Technical Report IS-GPS-200G, 2012.

[33] J. R. Wertz, W. J. Larson, Space Mission Analysis and Design, 3rd ed., Torrance, CA: Microcosm Press, 1999.

[34] W. Soh, M. Swartz, T. Patel, HEO AODCS Simulator Development and Validation Report, Technical Report ER104011, Magellan Aerospace, Winnipeg, 2013.

[35] L. R. Weill, GNSS Solutions: differences between signal acquisition and tracking, InsideGNSS 6 (2011).

[36] C. Jayles, J.-P. Chauveau, F. Rozo, DORIS/Jason-2: Better than 10 cm on-board orbits available for near-real-time altimetry, Advances in Space Research 46 (2010) 1497–1512.

[37] V. B. Mendes, R. B. Langley, Tropospheric zenith delay prediction accuracy for airborne GPS high-precision positioning, in: Proceedings of the Institute of Navigation 54th Annual Meeting, 1998, pp. 337–347.

[38] A. Reichert, T. Meehan, T. Munson, Toward decimeter-level real-time orbit determination: a demonstration using the SAC-C and CHAMP spacecraft, in: Proceedings of the 15th International Technical Meeting of the Satellite Division of The Institute of Navigation (ION GPS 2002), Portland, OR, 2002.

[39] Y. Bar-Sever, L. Young, F. Stocklin, J. Rush, NASA's global differential GPS system and the TDRSS augmentation service for satellites, in: Proceedings of the 2nd ESA Workshop on Satellite Navigation User Equipment Technologies, ESTEC, 2004.

[40] W. Soh, HEO STDP Navigation Trade-Off & Feasibility Study, Technical Report ER103975, Magellan Aerospace, Winnipeg, 2014.

[41] C. T. Kühl, Combined Earth-/Star Sensor for Attitude and Orbit Determination of Geostationary Satellites, Ph.D. thesis, Universität Stuttgart, 2005.

[42] L. Qiao, S. Lim, C. Rizos, J. Liu, GNSS-based orbit determination for highly elliptical orbit satellites, in: Proceedings of the International Symposium on GPS/GNSS 2009, Jeju, 2009.

[43] J. L. Crassidis, J. L. Junkins, Optimal Estimation of Dynamic Systems, 2nd ed., Boca Raton, FL: CRC Press LLC, 2011.

[44] D. Simon, Optimal State Estimation: Kalman, H Infinity, and Nonlinear Approaches, 1st ed., Hoboken, NJ: John Wiley & Sons, Inc., 2006.

[45] E. A. Wan, R. van der Merwe, The Unscented Kalman Filter for nonlinear estimation, in: Proceedings of the IEEE Symposium on Adaptive Systems for Signal Processing, Communications, and Control, Lake Louise, AB, 2000, pp. 153–158.

[46] S. Särkkä, On Unscented Kalman Filtering for state estimation of continuous-time nonlinear systems, IEEE Transactions on Automatic Control 52 (2007) 1631–1641.

[47] J. C. Butcher, A history of Runge-Kutta methods, Applied Numerical Mathematics 20 (1996) 247–260.

[48] MATLAB Documentation Centre, Solve nonstiff differential equations, medium order method - MATLAB ode45, accessed 08 April 2014. URL: http://www.mathworks.com/help/matlab/ref/ode45.html.

[49] P. Zentgraf, S. Berge, C. Chasset, H. Filippi, E. Gottzein, I. Gutiérrez-Cañas, M. Hartrampf, P. Krauss, C. Kuehl, B. Lübke-Ossenbeck, M. Mittnacht, O. Montenbruck, C. Müller, P. Rueda Boldo, A. Truffi, Preparing the GPS-experiment for the Small GEO mission, in: Proceedings of the 33rd AAS Guidance and Control Conference, Breckenridge, CO, 2010.

[50] United States Coast Guard, Navstar GPS user equipment introduction, Technical Report, U.S. Coast Guard Navigation Center, Alexandria, VA, 1996.

[51] E. A. Wan, R. van der Merwe, Chapter 7: The Unscented Kalman Filter, in: S. Haykin (Ed.), Kalman Filtering and Neural Networks, New York: John Wiley & Sons, Inc., 2001, pp. 221–280.